Proceedings of the Fifteenth International Conference on
Computational Structures Technology
Edited by: P. Iványi, J. Kruis and B.H.V. Topping
Civil-Comp Conferences, Volume 9, Paper 8.2
Civil-Comp Press, Edinburgh, United Kingdom, 2024
ISSN: 2753-3239, doi: 10.4203/ccc.9.8.2

Buckling Optimization of Variable-Stiffness Composite Plates with Two Circular Holes using Potential Flow and Conformal Mapping

Z. Jing

School of Aeronautics, Northwestern Polytechnical University
Xi'an, Shaanxi Province, China

Abstract

Potential flow around two equal-radius cylinders is derived analytically and applied to generate the curvilinear fiber path of variable-stiffness composite plates with two circular holes. As complex variable theory and conformal mapping are used to generate the potential flow around two equal-radius cylinders, the location and size of the two equal-radius circular holes are arbitrary. By changing the angle of incoming flow, the global fiber angle of a variable-stiffness lamina can be simulated and the local fiber orientation angle at any point is determined by the global potential flow field. Buckling performance of variously-shaped variable-stiffness composite plates with two circular holes are studied via discrete Ritz method. A three-dimensional sampling optimization method is then adopted to optimize the curvilinear fiber configurations of variable-stiffness composite plates, and its buckling performances are compared with those of constant stiffness composites with straight fibers. Significant improvements on load-carrying capacity can be achieved compared to straight ones, demonstrating that using potential flow is one of the most efficient way to generate curvilinear optimal fiber path with maximum load-carrying capacity for variable-stiffness composite plates with material discontinuity. Moreover, discrete Ritz method exhibits good precision and stability for buckling analysis of variable-stiffness composite plates with complex geometries.

Keywords: discrete Ritz method, potential flow, conformal mapping, variable-stiffness composite plates, buckling, optimization.

1 Introduction

With the mature of advanced manufacturing techniques such as automated fiber placement and additive manufacturing, it is possible to define the fiber path in a curvilinear manner with highly flexible design freedoms, producing variable-stiffness composite structures that may significantly enhance structural efficiency. As the fiber path of variable-stiffness composites (VSC) can be continuously altered within the plate domain, VSC provide the possibility to tailor the stiffness of structures at a point-by-point level. Consequently, VSC structures exhibit superior performance in load-carrying capacity situations when compared with constant-stiffness composites (CSC) with straight fibers. It is demonstrated that the buckling load of composite fuselage panels improved as higher as 78% [1] as compare to quasi-isotropic laminates, and the weight of aircraft wings can be reduced about 20% [2] when using VSC as compare to CSC. The load-carrying capacity enhancement and weight reduction potential of VSC promote it to be the best lightweight material for the next generation aerospace engineering.

Aircraft structures such as fuselages and wings have cutouts or openings that sever as windows and doors, or ensure electrical, fuel, and hydraulic lines are accessible for maintenance and reduce the weight of structures. Cutouts in such thin-walled composite structures may cause material discontinuity and stress concentration, alter the mass and stiffness of the structure, and hence significantly change the buckling and failure performances. Understanding the buckling behavior and improve its load-carrying capacity is of great importance for their practical application in engineering. Curving the fibers smoothly and continuously within the layer provides an advanced tailoring option to account for material discontinuities and non-uniform stress states, as well as modifying the principal load paths to enhance load-carrying capacity [2].

In general, two main strategies are adopted for generating the continuous fiber trajectories around cutouts: using potential flow function or along the vectors' directions of maximum principal stresses. The potential flow can generate perfect streamlines around cutouts with relatively simple geometries, e.g. circular or elliptical. With more complex geometries in real engineering structures, the analytical potential flow may be difficult to derive or even impossible. The maximum principal stress can be easily obtained by FEM, but their vectors need to be regulated by specialized algorithm to generate smooth and continuous fiber path around holes. Actually, the potential flow in fluid mechanics and the stress field in elasticity can be solved by the complex variable theory. Recent literatures reported that the potential flow around multiple circular cylinders [3-8] and polygonal shaped cylinders [9] can be calculated analytically. Moreover, engineering structures with multiple cutouts and complex geometries are commonly encountered, few studies investigated the VSC plates with multiple holes and complex geometries. One obstacle is the generation of complex potential flow for characterizing curvilinear fiber path, and another difficulty is the numerical simulation of plates with complex geometries, which requires re-formulation and analysis of FEM.

Considering the advantages of potential flow for constructing the continuous fiber path over cutouts and the convenience of discrete Ritz method (DRM) [13, 14] for solving mechanical problems in an arbitrarily geometrical domain, this study derived analytical potential flow to generate the curvilinear fiber trajectories around two equal-radius circular holes and conducted DRM based buckling analysis for variously-shaped VSC plates with two circular holes. Standard buckling formulas for arbitrarily shaped VSC plates are derived, and convergence and accuracy of DRM are investigated and verified with previous studies. After that, three-dimensional sampling optimization (3DSO) method [10] based optimization is conducted for maximization of buckling load of VSC plates with different boundary conditions and loadings. Optimal results are compared to those of CSC plates with straight fibers.

2 Fiber path characterization based on potential flow

Complex variable theory is an important mathematical tool for the study of inviscid irrotational fluid flow, otherwise known as potential flow. There are a number of applications for potential flow, including describing the velocity field on aerofoils, groundwater flow, water waves, electro-osmotic flow, etc. Using Milne-Thomson circle theorem [3, 4], complex potential functions can be derived to model uniform potential flow around a circular cylinder and non-uniform potential flow due to a singular point outside the cylinder. However, modelling the fluid flow over multiple cylinders is more complicated. Recent studies [5-8] show that the potential flow around two equal-radius cylinders can be computed analytically. As streamline represents an instantaneous tangent path of a massless particle moving with the flow [1], it is the contour of the flow velocity field. In order to calculate the local fiber orientation angles in a variable stiffness lamina, the components of the velocity field must be calculated.

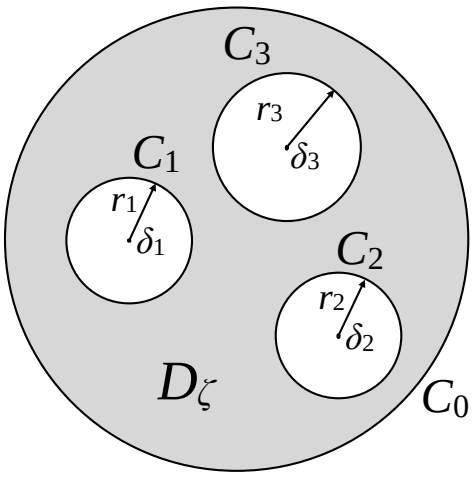

Figure 1: A multiply connected circular domain D_ζ with smaller circular discs

Let D_ζ be a unit multiply connected circular domain, defined by $|\zeta| = 1$ ($\zeta \in \square$), with M smaller circular disks excised. The boundary of the unit circle D_ζ is C_0 and the boundaries of M smaller circular discs enclosed by C_0 are $\{C_j \mid j = 1, 2, \ldots, M\}$. Let

the center and radius of C_j be denoted by $\delta_j \in \square$ and $r_j \in \square$, respectively, as shown in Figure 1. In general, such circular domains are canonical types of multiply connected domains [11], and some kind of bounded multiply connected circular domain D_ζ can be conformally mapped (by some function $z(\zeta)$) to an unbounded fluid region D_z outside of any given set of obstacles [6, 9].

Let $-(i/2\pi)W_0(\zeta, \beta)$ be the complex potential associated with an incompressible flow in D_ζ which is irrotational except for a single point vortex singularity at $\zeta = \beta$. Assume all circulations around the inner circular discs are zero. The function $W_0(\zeta, \beta)$ is analytic everywhere in D_ζ except for a logarithmic singularity at $\zeta = \beta$ corresponding to the point vortex. Such that

$$\mathrm{Re}[W_0(\zeta,\beta)] = 0, \quad \text{on } |\zeta| = 1 \tag{1}$$

and

$$\mathrm{Re}[W_0(\zeta,\beta)] = c_j, \quad \text{on } C_j, \quad j = 1, 2, ..., M \tag{2}$$

where c_j are real constants. The above conditions ensure that all boundaries are streamlines. In this case, selection Equation (1) provides a normalization that uniquely identifies $W_0(\zeta, \beta)$.

Crowdy and Marshall [5] demonstrated that the following complex potential $W_0(\zeta, \beta)$ satisfies all above conditions:

$$W_0(\zeta,\beta) = \log\left(\frac{\omega(\zeta,\beta)}{|\beta|\,\omega(\zeta,\bar{\beta}^{-1})}\right) \tag{3}$$

where $\omega(\zeta, \beta)$ is a function of two complex variables, and it is a classical infinite product formula defined as [6, 7, 12]:

$$\omega(\zeta,\beta) = (\zeta-\beta)\prod_{\phi_k}^{\infty}\frac{(\phi_k(\zeta)-\beta)(\phi_k(\beta)-\zeta)}{(\phi_k(\zeta)-\zeta)(\phi_k(\beta)-\beta)} \tag{4}$$

where the product is over all compositions of the basic Möbius maps [6] { $\{\phi_k, \phi_k^{-1} \mid k = 1, 2, ..., M\}$ (M is the number of smaller discs in domain D_ζ) excluding the identity and all inverse maps.
In the doubly connected case, D_ζ is taken to be a concentric annulus $r < |\zeta| < 1$ with $0 < r < 1$, and there is only one Möbius map $\phi_1(\zeta) = r^2\zeta$. Accordingly, the infinite product Equation (4) is then over all mappings of the form:

$$\{\phi_k(\zeta) = r^{2k}\zeta \mid k \geq 1\} \tag{5}$$

Substitute Equation (5) into Equation (4) yields:

$$\omega(\zeta,\beta) = -\frac{\beta}{C^2}F\left(\frac{\zeta}{\beta}, r\right) \tag{6}$$

where

$$\begin{cases} F(\zeta,r)=(1-\zeta)\prod_{k=1}^{\infty}(1-r^{2k}\zeta)(1-r^{2k}\zeta^{-1}) \\ C=\prod_{k=1}^{\infty}(1-r^{2k}) \end{cases} \tag{7}$$

Substitute Equations (6) and (7) into Equation (3) yields:

$$W_0(\zeta,\beta)=\log\left(\frac{F(\zeta\beta^{-1},r)}{|\beta|F(\zeta\bar{\beta},r)}\right) \tag{8}$$

Moreover, it is known that the required complex potential for uniform flow with speed U_0 in a direction making angle α with the positive real axis is given by [27]:

$$W_1(\zeta,\beta)=U_0\left[e^{i\alpha}\frac{\partial}{\partial\bar{\beta}}-e^{-i\alpha}\frac{\partial}{\partial\beta}\right]W_0(\zeta,\beta) \tag{9}$$

Substitute Equation (8) into Equation (9) yields:

$$W_1(\zeta,\beta)=\frac{iU_0}{\beta}\sin\alpha+\frac{U_0}{\beta}\left[e^{i\alpha}K(\zeta\beta^{-1},r)-e^{-i\alpha}K(\zeta\beta,r)\right] \tag{10}$$

where β is taken to be real and set as $\beta = r^{1/2}$, and where we define

$$K(\zeta,r)=\frac{\zeta}{F(\zeta,r)}\frac{\partial F(\zeta,r)}{\partial\zeta} \tag{11}$$

As the first term in Equation (10) is a constant, it is discarded.

Lastly, the streamlines for steady uniform flow around two equal circular cylinders can be obtained by using the Möbius conformal mapping from the annulus $r < |\zeta| < 1$:

$$Z(\zeta)=R\left(\frac{\zeta+\sqrt{r}}{\zeta-\sqrt{r}}\right) \tag{12}$$

where R is a real constant and taken as $R = r^{1/2}$. By using the above conformal mapping, the annulus $r < |\zeta| < 1$ can always be mapped to two equal-radius cylinders both centered along the real-axis and symmetrically disposed about the origin. R and r are real parameters which determine the radius of each cylinder and the distance between them. Moreover, if the parameter r is taken as a pure imaginary number, the size and location of the two equal-radius cylinders will alter.

The complex velocity around the two circular cylinders can be obtained in terms of the complex potential function [9, 11]:

$$V_c=u_c-iv_c=\frac{dW_1(\zeta,\beta)}{d\zeta}\Big/\frac{dZ}{d\zeta} \tag{13}$$

where u_c and v_c are the real and imaginary components of complex velocity V_c respectively, which are the function of coordinate (x, y) in the complex plane. Figure. 2 depicts the streamlines for steady uniform flow around two equal circular cylinders with $\alpha = 0°$.

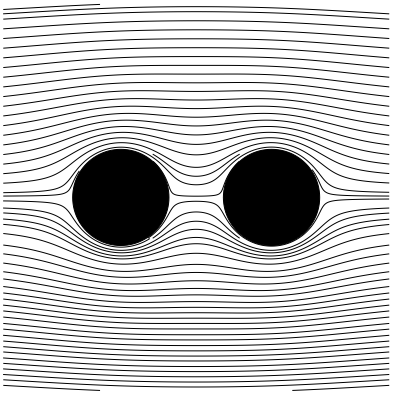

Figure 2: Streamlines for steady uniform flow around two equal circular cylinders

Consider the variable stiffness laminate with two circular holes, the streamlines constructed above are the fiber path of a lamina. The angle α in Equation (10) represents the global fiber orientation of a lamina. The local fiber orientation angle θ at any point (x, y) in the complex plane can be calculated via:

$$\theta(x, y) = \arctan\left(\frac{v_c(x, y)}{u_c(x, y)}\right) \tag{14}$$

Figure 3 demonstrates the fiber paths of variable-stiffness laminas with different global fiber orientation α and its corresponding local fiber orientation angle θ.

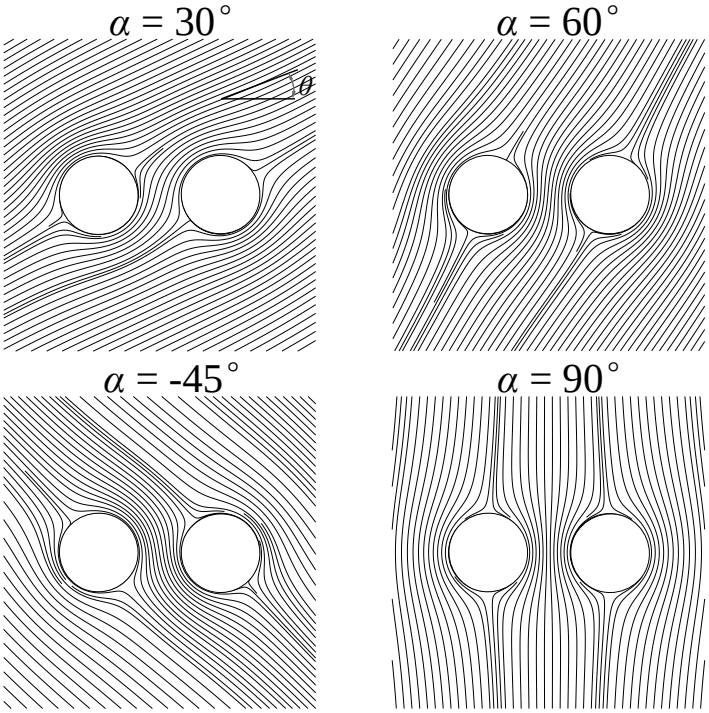

Figure 3: Variable-stiffness laminas with different global fiber orientation α and its corresponding local fiber orientation angle θ for the VSC plates with two circular holes

3 Numerical results

In all of the following examples, composite material properties are given as: E_1 = 130GPa, E_2 = 10GPa, $G_{12} = G_{13} = G_{23}$ = 5GPa, v_{12} = 0.35, and ply thickness is t = 0.15mm. Accounting for different boundary conditions and loadings, stacking configurations of variously-shaped VSC plates with two equal-radius circular holes are optimized to maximize the critical buckling load, including square and triangular plates. The three-dimensional sampling optimization (3DSO) method is used to perform buckling optimization [10]. Two kinds of symmetrical VSC plates are considered: 16-layer and 48-layer laminate with interval of ply orientation 5°. The number of objective function calls is denoted by *NF*. Optimal buckling results and mode shapes are provided.

3.1 Square plates with two circular holes

A square VSC plate having dimensions $a = b$ = 120mm, with two equal-radius circular holes located at O_1(-26.4mm, 0) and O_2(26.4mm, 0) with radius r_0 = 16.2mm, subjected to axial compressive and shear loads (single or combined), under simply supported (SSSS) or clamped (CCCC) boundary conditions on four edges, are presented in Figure 4a. 60×60 Gauss points are used to discretize the VSC plate, where 10×10 meshes are generated and each background mesh consists of 6×6 Gauss points, the discretization model is shown in Figure 4b. The Gauss points in the two circular holes are with zero stiffness. Convergence study for the square VSC plate $[45/-45_2/45/-45/40/90_2]_s$ under SSSS boundary condition is presented in Table 1. Increasing the number of terms in the Legendre polynomials from 12×12 to 19×19 results in convergent results for the first eight buckling load factors. Accounting for both efficiency and accuracy of the buckling analysis, 18×18 terms are used in the Legendre polynomials for optimization. The inplane stress resultants ($\bar{N}_x, \bar{N}_y, \bar{N}_{xy}$) of the square VSC plate $[45/-45_2/45/-45/40/90_2]_s$ with two circular holes, under SSSS boundary condition, subjected to uniaxial compression, are presented in Figure 5, and compare with those of FEM results. The stress concentration occurs around the boundaries of the two holes, and the present DRM results are in excellent agreement with those of FEM, verifying the accuracy of DRM for prediction of inplane deformation.

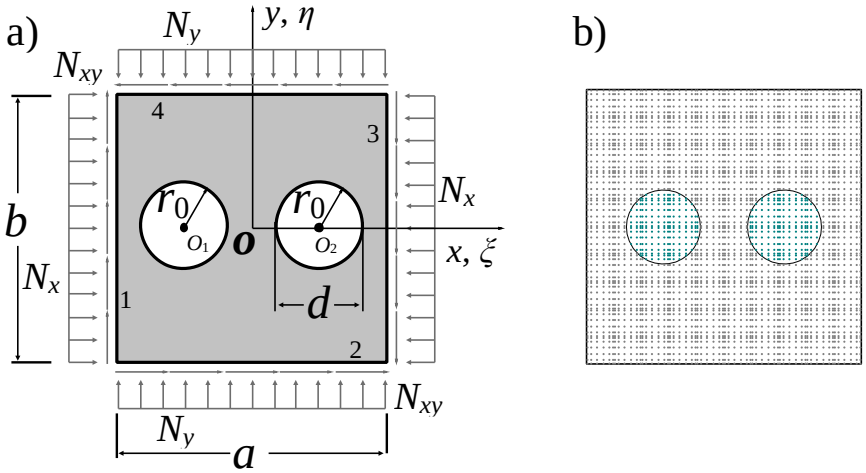

Figure 4: Geometry and discretization models of square VSC plate with two circular holes: a) Geometric model and loading; b) Discretization model (green points are with zero stiffness)

Buckling optimal results are presented in Table 2, and compare with optimal results of CSC with straight fibers. A significant improvement in the buckling loads of optimal VSC plates with potential flow-based curvilinear fiber paths has been demonstrated as high as 22.59%. Figure 6 illustrates some of the first four optimal buckling mode shapes for VSC plates. Lastly, the optimal buckling results of 48-layer symmetrical VSC plates under uniaxial, biaxial compression, combined loading are shown in Table 3. According to Tables 2 and 3, the computational cost of a 48-layer laminate is approximately three times that of a 16-layer laminate, which indicates that computation expenses for 3DSO method are almost linearly related to the number of layers in the laminate, since sampling does not scale exponentially with increasing design variables. In Figure 7, a convergence picture is shown for a 48-layer square VSC plate subjected to uniaxial compression under CCCC boundary condition. The sampling optimum is extremely close to the final optimum.

Solution size ($\tilde{M}\times\tilde{N}$)	Mode							
	1	2	3	4	5	6	7	8
12×12	17.7641	22.3389	31.3671	41.3625	47.6108	48.7098	64.3150	69.4361
14×14	17.7924	22.2795	31.3702	40.2842	47.0341	47.7262	64.4736	67.8380
16×16	17.8200	22.2753	31.4484	39.6329	46.8073	46.9710	64.9073	67.0888
17×17	17.8385	22.2641	31.4212	39.4054	46.7364	46.8412	64.8695	66.9171
18×18	17.8281	22.2487	31.3591	39.1951	46.5287	46.8145	64.7773	66.8632
19×19	17.8416	22.2469	31.3505	39.0509	46.3767	46.8031	64.7771	66.7736
FEM	17.8943	22.1254	31.4977	37.8240	45.0400	46.6043	63.9963	66.2121

Table 1: Convergence of first eight buckling load factors $\lambda = \lambda_{cr}b^2/D_0$ for the 16-layer square VSC plate $[45/-45_2/45/-45/40/90_2]_s$ with two circular holes, under SSSS boundary condition, subjected to uniaxial compression

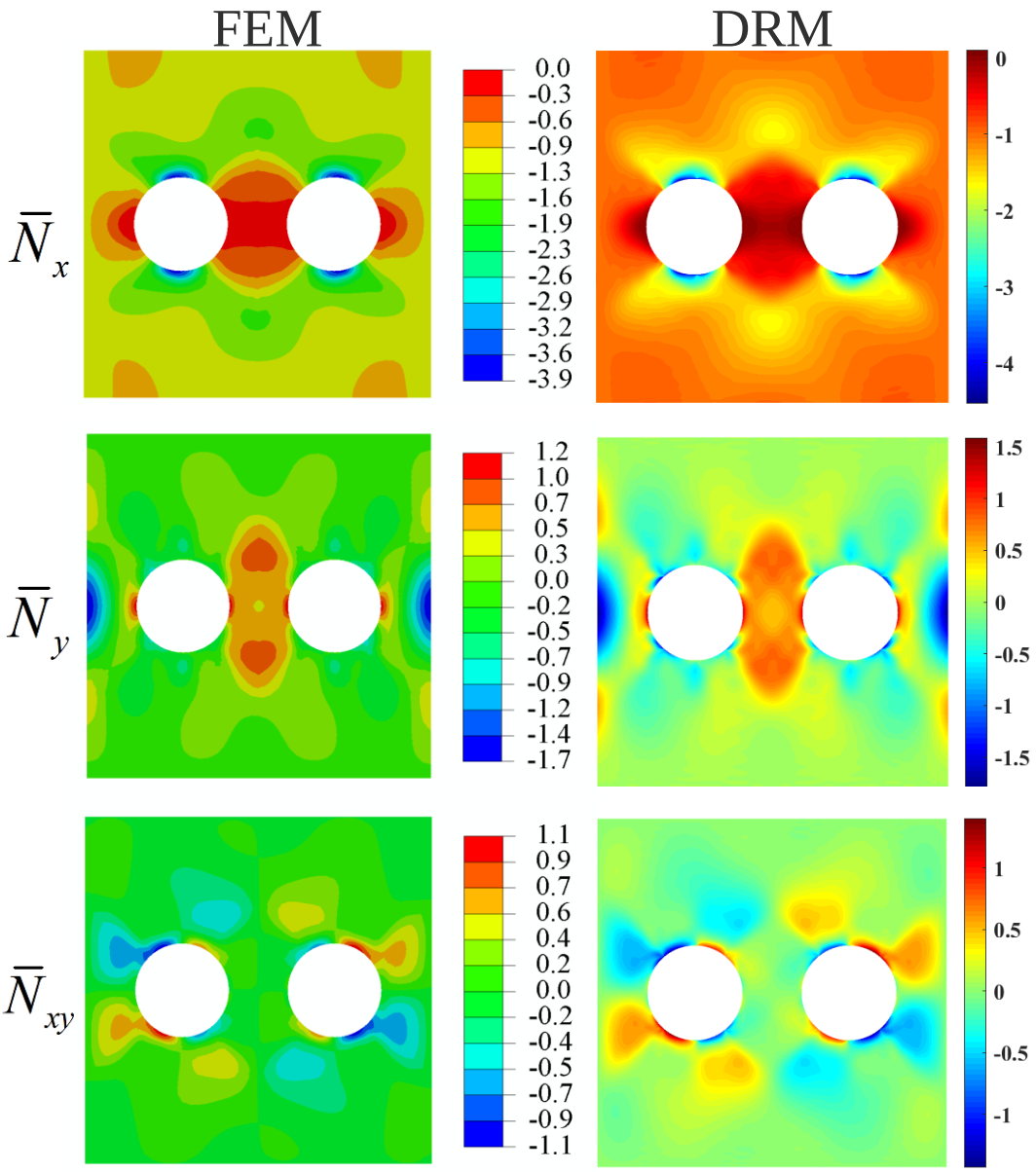

Figure 5: Inplane stress resultants ($\bar{N}_x, \bar{N}_y, \bar{N}_{xy}$) of the square VSC plate [45/-45$_2$/45/-45/40/90$_2$]$_s$ (curvilinear fiber path) with two circular holes, under SSSS boundary condition, subjected to uniaxial compression, and compare with FEM results.

Load (N/mm)	BC	VSC plates			Increase (%)
		$\mathbf{\Phi}_{opt}$	λ_{opt}	*NF*	
Uniaxial compression	SSSS	$[45/-45_2/45/-45/40/90_2]_s$	17.828	776	15.69
	CCCC	$[0/-80/0_3/70/-80/80]_s$	43.937	1144	9.51
Biaxial compression	SSSS	$[50/-50/-45/45/-45/-45/40_2]_s$	8.2086	1104	20.23
	CCCC	$[-65/80/50/50/-35/-35/-35/50]_s$	16.959	1144	0.32
Biaxial compression and shear	SSSS	$[45_2/-50_2/40/-55/35/-65]_s$	8.0330	1024	22.59
	CCCC	$[35_2/90/-85_2/30_2/-80]_s$	16.757	1272	4.61

Load (N/mm)	BC	CSC plates			Increase (%)
		$\mathbf{\Phi}_{opt}$	λ_{opt}	*NF*	
Uniaxial compression	SSSS	$[40/-40/45/-45/-50/-55/70/85]_s$	15.411	1340	15.69
	CCCC	$[-10/20/15/-55/-70/65_2/-80]_s$	40.120	1104	9.51
Biaxial compression	SSSS	$[45/-45/-45/50/-50/50/90_2]_s$	6.8276	1652	20.23
	CCCC	$[-70/70/90/30/-55/65/80/75]_s$	16.905	1588	0.32
Biaxial compression and shear	SSSS	$[-50/45/50_2/-45_2/-35/-80]_s$	6.5529	1468	22.59
	CCCC	$[65/30/80/85/-85/-40_3]_s$	16.018	1676	4.61

Table 2: Optimal buckling load factor $\lambda_{opt} = \lambda_{cr}b^2/D_0$ of 16-layer square VSC and CSC plates with two circular holes

Load (N/mm)	BC	VSC plates (curvilinear fiber path)		
		$\mathbf{\Phi}_{opt}$	λ_{opt}	*NF*
Uniaxial compression	SSSS	$[(-45/45)_2/45/-45_3/45_4/(-40/45)_2/-40/90_6/-40]_s$	14.260	4520
	CCCC	$[5/-10/5/0_3/-70/75/0_3/-75/0_3/75/80_2/-80/80/-80_2/80/-80]_s$	29.675	4480
Biaxial compression ($N_x/N_y = 1$)	SSSS	$[-50_2/50_4/45/-50/45/-45_5/45/-45_3/40_2/-40/40_3]_s$	6.6734	3616
	CCCC	$[-85/90_3/20/-15/90_5/0_4/(90/0)_2/0_4/90]_s$	13.463	2792
Biaxial compression and shear ($N_x/N_y = N_{xy}/N_y = 1$)	SSSS	$[-50/45_6/-50/40/-55/40_4/-55_2/-60/35/-65_6]_s$	6.3940	4812
	CCCC	$[30_2/90/30_2/-85_2/30_2/-85_2/30_5/-80_8]_s$	11.885	3696

Table 3: Optimal buckling load factor $\lambda_{opt} = \lambda_{cr}b^2/D_0$ of 48-layer square VSC plates with two circular holes

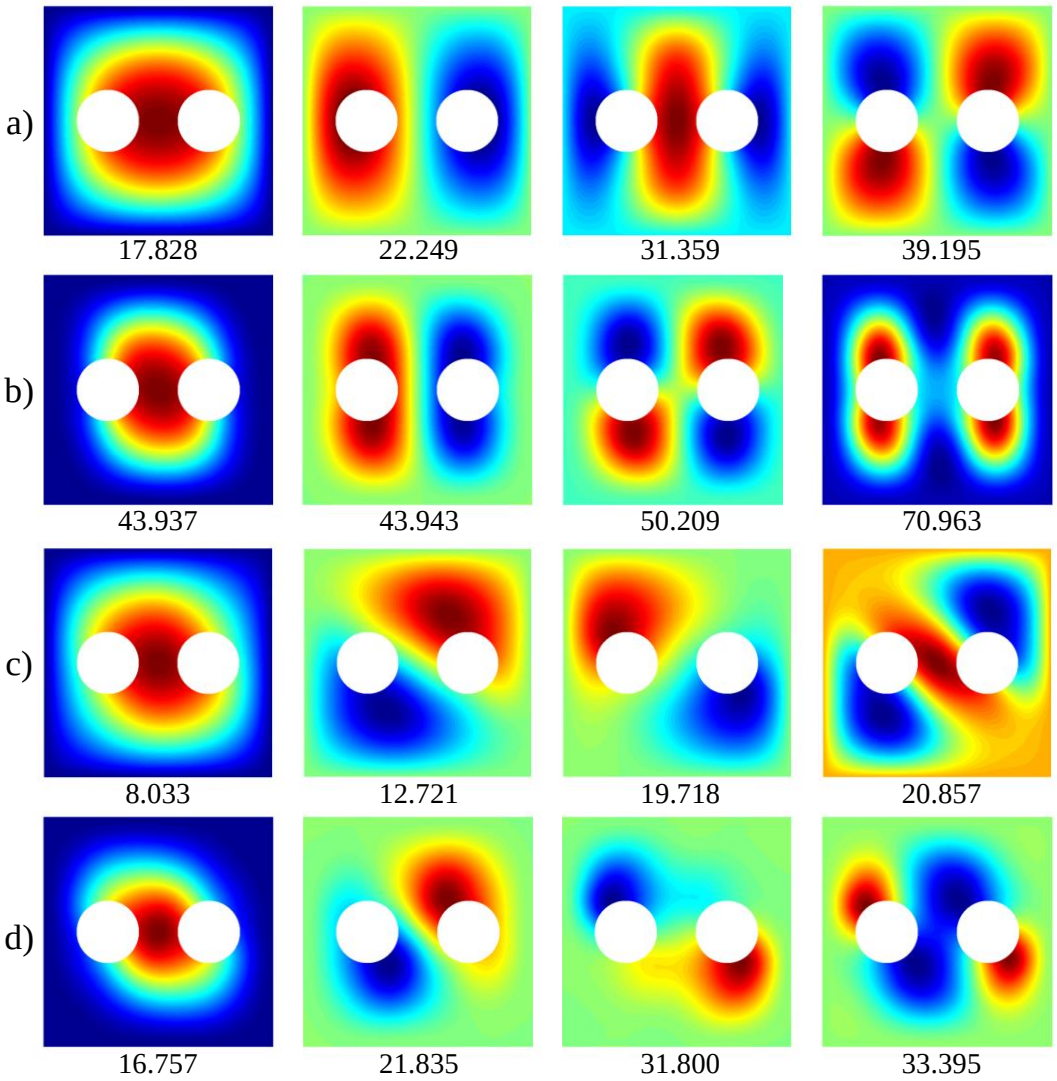

Figure 6: First four mode shapes of the optimal square VSC plates: a) $[45/-45_2/45/-45/40/90_2]_s$ with SSSS boundary under uniaxial compression; b) $[0/-80/0_3/70/-80/80]_s$ with CCCC boundary under uniaxial compression; c) $[45_2/-50_2/40/-55/35/-65]_s$ with SSSS boundary under biaxial compression and shear; d) Clamped $[35_2/90/-85_2/30_2/-80]_s$ with CCCC boundary under biaxial compression and shear.

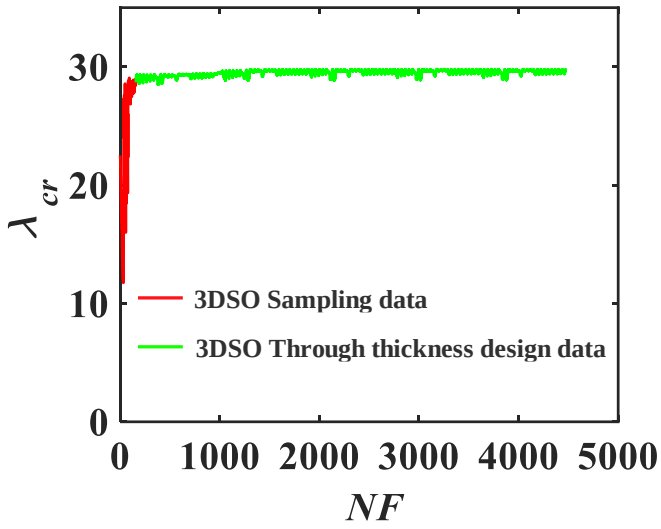

Figure 7: Convergence process of 3DSO for optimization of the 48-layer square VSC plate with two circular holes, under CCCC boundary condition, subjected to uniaxial compression

3.2 Triangular plates with two circular holes

A triangular VSC plate having three vertices located at (x_1, y_1) = (-60, -60)mm, (x_2, y_2) = (60, -60)mm, (x_3, y_3) = (0, 60)mm, with two equal-radius circular holes located at O_1(-4.2, 0)mm and O_2(16.2, -29.4)mm with radius r_0 = 11.52mm, subjected to uniform compressive load N on all edges, under simply supported (SSS) or clamped (CCC) boundary conditions on three plate edges, is presented in Figure 8a. The smallest rectangular domain to cover the triangular VSC plate has dimensions of a = b = 120mm, and the rectangular domain is regarded as a variable stiffness system with zero stiffness in the cutout domain and nonzero stiffness in the triangular plate domain. As shown Figure 8b, 80×80 Gauss points are used to discretize the perforated triangular VSC plate. In Table 4, convergence study is performed for the triangular VSC plate $[-35/-30/75/40/-10/55/65/75]_s$ with two circular holes under SSS boundary condition. As the number of terms increases from 12×12 to 19×19, the first eight buckling load factors converge. Accordingly, 17×17 terms are used in DRM in order to ensure the accuracy of the buckling analysis and optimization. In Figure 9, the inplane stress resultants ($\bar{N}_x, \bar{N}_y, \bar{N}_{xy}$) of the triangular VSC plate $[90/10/0/-85/-55/80/60/-60]_s$ with two circular holes, under clamped boundary condition, subjected to uniform compressive load N, are compared with those of FEM results. It is observed that the stress concentration occurs around the two holes and between one hole and the edge of the triangular plate, and the inplane stress resultants of DRM are in accordance with those obtained by FEM. Demonstrating the accuracy of DRM in predicting the inplane deformation behavior of triangular VSC plates with complex geometries.

Solution size ($\tilde{M}\times\tilde{N}$)	Mode							
	1	2	3	4	5	6	7	8
12×12	15.0087	30.1965	35.2108	46.8037	53.1342	60.7267	72.1749	77.5758
14×14	14.9166	29.9930	34.9033	46.1550	52.4161	59.6768	72.6348	77.1266
16×16	14.8395	29.7958	34.6934	45.6666	51.9519	59.1407	68.0215	73.0456
17×17	14.7967	29.6628	34.5905	45.4742	51.7620	58.8830	73.0546	76.2546
18×18	14.7693	29.6047	34.5503	45.2866	51.5383	58.7250	73.0835	75.9781
19×19	14.7468	29.5239	34.5035	45.1269	51.4616	58.5789	73.0624	75.7712
FEM	14.4845	29.0460	34.3117	44.1772	50.6877	57.9848	72.2207	74.5944

Table 4: Convergence of the first eight buckling load factors $\lambda = \lambda_{cr}b^2/D_0$ for the 16-layer triangular VSC plate $[-35/-30/75/40/-10/55/65/75]_s$ with two circular holes, under SSS boundary condition, subjected to uniform compressive load N on all edges

Optimal buckling results for triangular VSC plates are reported in Table 5 and are compared with those of the CSC optimal results with straight fibers. The use of curvilinear fiber paths constructed on potential flow results in approximately 25% improvement on buckling load. There is no doubt that fiber trajectory around circular holes improves load transfer efficiency. The first four buckling mode shapes for the optimal triangular VSC plates in Table 5 are shown in Figure 10. The optimal curvilinear fiber paths for the VSC plate $[90/10/0/-85/-55/80/60/-60]_s$ are demonstrated in Figure 11.

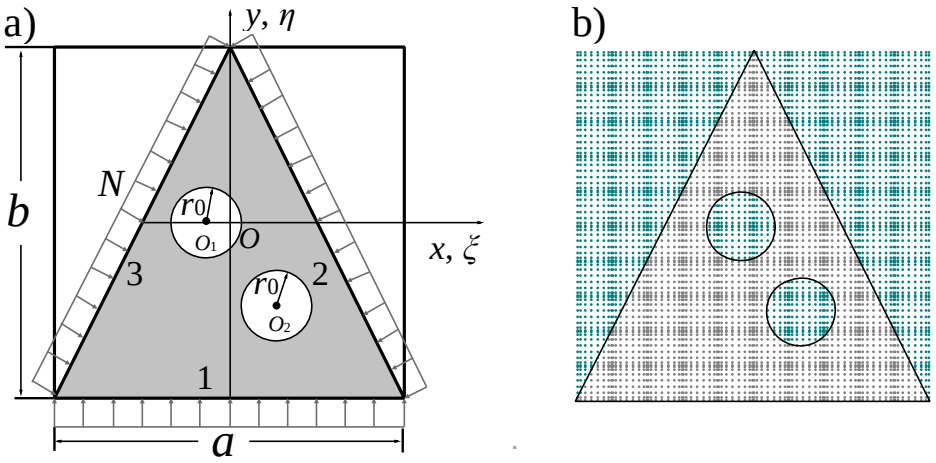

Figure 8: Geometry and discretization models of triangular VSC plate with two circular holes: a) Geometric model and loading; b) Discretization model

BC	VSC plates (curvilinear fiber path)			CSC plates			Increase (%)
	$\mathbf{\Phi}_{opt}$	λ_{opt}	*NF*	$\mathbf{\Phi}_{opt}$	λ_{opt}	*NF*	
SSS	$[-35/-30/75/40/-10/55/65/75]_s$	14.840	816	$[35/-40/-45/75/0/60_2/45]_s$	11.825	856	25.13
CCC	$[90/10/0/-85/-55/80/60/-60]_s$	36.072	736	$[0/90/0_4/90/0]_s$	29.963	696	20.39

Table 5: Optimal buckling load factor $\lambda_{opt} = \lambda_{cr}b^2/D_0$ of 16-layer triangular VSC and CSC plates with two circular holes

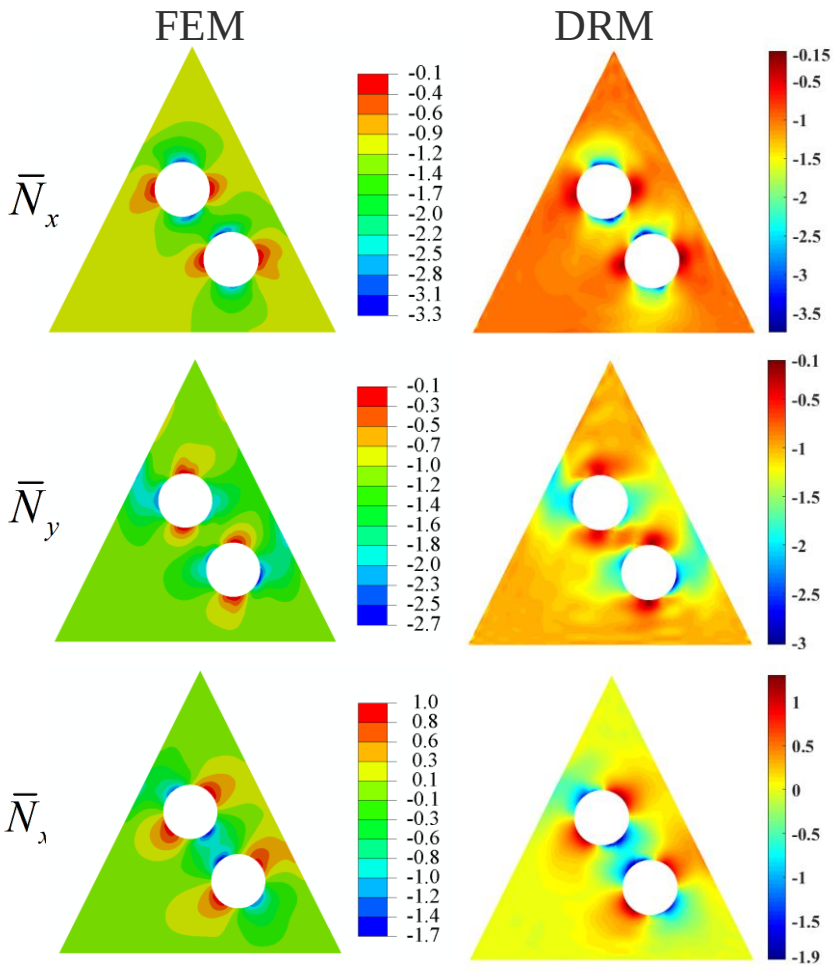

Figure 9: Inplane stress resultants ($\bar{N}_x, \bar{N}_y, \bar{N}_{xy}$) of the triangular VSC plate [90/10/0/-85/-55/80/60/-60]$_s$ (curvilinear fiber path) with two circular holes, under CCC boundary condition, subjected to uniform compressive load *N*, and compare with FEM results.

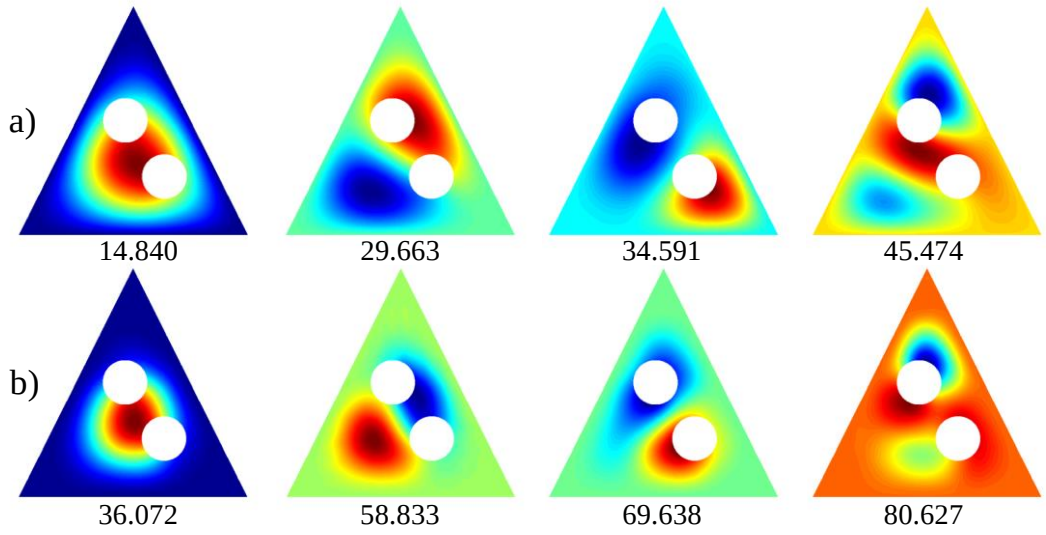

Figure 10: First four buckling mode shapes of the optimal triangular VSC plates: a) $[-35/-30/75/40/-10/55/65/75]_s$ with SSS boundary; b) $[90/10/0/-85/-55/80/60/-60]_s$ with CCC boundary.

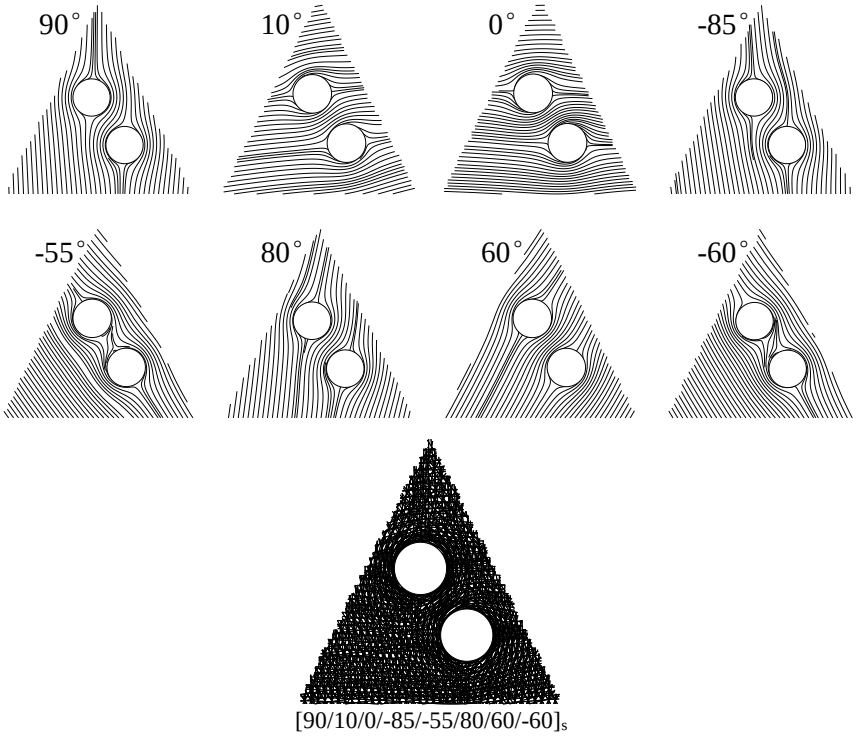

Figure 11: Optimal curvilinear fiber paths $[90/10/0/-85/-55/80/60/-60]_s$ with CCC boundary condition

4 Conclusions and Contributions

The potential flow around two equal-radius circular cylinders are derived and applied to generate the curvilinear fiber paths of VSC plates with two circular holes. By changing the incoming flow angle of potential flow, the global fiber angle orientation for an individual layer can be simulated and the local fiber angle can be obtained at any point in the plate domain in terms of the global potential flow field. DRM is developed for buckling analysis of perforated VSC plates, and convergence and accuracy of DRM are compared and verified with previous results as well as FEM. DRM can provide high precision results with relatively low degree of freedom as a global trial function is used. Moreover, as extended interval integral and Gauss quadrature are used within a rectangular domain for numerical integration, with sufficient Gauss points, integration over an arbitrarily shaped plate can be realized by using variable stiffness within the cutouts in the rectangular domain. In this manner, the energy formulas and computation procedures of DRM are standard, making it powerful to solve the static and buckling problem of VSC plates in arbitrary geometries. 3DSO is adopted to perform stacking configurations optimization of VSC plates and CSC plates, and comparison results indicate that the potential flow based curvilinear fiber paths significantly improve the buckling load-bearing capacity of VSC plates as compare to CSC plates. As complex potential flow can generate continuous fiber path over complex geometric domain, it exhibits potential for further application to more complex 2D and 3D problems for design optimization of VSC structures.

Acknowledgements

This work is supported by the National Natural Science Foundation of China (No. 12102352), Qin Chuang Yuan Construction of Two Chain Integration Special Project (No. 23LLRH0002), Fundamental Research Funds for the Central Universities (No. G2023KY0605).

References

[1] A. Alhajahmad, C. Mittelstedt, “Buckling and postbuckling performance of composite fuselage panels with cutouts using continuous streamline fibres”, International Journal of Mechanical Sciences, 212, 106841, 2021.

[2] T. Brooks, “Design Optimization of Flexible Aircraft Wings Using Tow-steered Composites”, Michigan, 2018.

[3] L. Milne-Thomson, Theoretical Hydrodynamics, Macmillan, 1968.

[4] D. J. Acheson, “Elementary Fluid Dynamics”, Oxford University Press, 1990.

[5] D. Crowdy, J. Marshall, “Analytical formulae for the Kirchhoff–Routh path function in multiply connected domains”, Proceedings of the Royal Society A: Mathematical, Physical and Engineering Sciences, 461(2060), 2477-2501, 2005.

[6] D.G. Crowdy, “Analytical solutions for uniform potential flow past multiple cylinders”, European Journal of Mechanics-B/Fluids, 25(4), 459-470, 2006.

[7] D.G. Crowdy, “A new calculus for two-dimensional vortex dynamics”, Theoretical and Computational Fluid Dynamics, 24(1), 9-24, 2010.

[8] D.G. Crowdy, “Uniform flow past a periodic array of cylinders”, European Journal of Mechanics-B/Fluids, 56, 120-129, 2016.

[9] D.T. Solanki, D.S. Sharma, “Potential flow around Polygonal Shaped Cylinders using Hypotrochoidal Mapping function”, International Journal of Mechanical Sciences, 226, 107395, 2022.
[10] Z. Jing, L. Duan, “A three-dimensional sampling optimization method for buckling optimization of variable prestressed composite plates”, Thin-Walled Structures, 181, 110096, 2022.
[11] Z. Nehari, “Conformal Mapping”, McGraw-Hill, New York, 1952.
[12] H.F. Baker, “Abelian functions: Abel’s theorem and the allied theory of theta functions”, Cambridge University Press, Cambridge ,1897.
[13] Z. Jing, “Variable stiffness discrete Ritz method for free vibration analysis of plates in arbitrary geometries”, Journal of Sound and Vibration, 553, 117662, 2023.
[14] Z. Jing, L. Duan, “Discrete Ritz method for buckling analysis of arbitrarily shaped plates with arbitrary cutouts”, Thin-Walled Structures, 193, 111294, 2023.